# Compatibility of quantitative X-ray spectroscopy with continuous distribution models of water at ambient conditions

**J. Niskanen[a,b], M. Fondell[a], Ch. J. Sahle[c], S. Eckert[d,a], R. M. Jay[d,a], K. Gilmore[c], A. Pietzsch[a], M. Dantz[e], X. Lu[e], D. McNally[e], T. Schmitt[e], V. Vaz da Cruz[f,a], V. Kimberg[f,g], F. Gel'mukhanov[f,g], and A. Föhlisch[a,d,1]**

[a]Helmholtz Zentrum Berlin für Materialien und Energie, Institute for Methods and Instrumentation for Synchrotron Radiation Research, Albert-Einstein-Str. 15, D-12489 Berlin, Germany; [b]University of Turku, Department of Physics and Astronomy, FI-20014 Turun yliopisto, Finland; [c]European Synchrotron Radiation Source,71 Avenue des Martyrs F-38000 Grenoble, France; [d]Universität Potsdam, Institut für Physik und Astronomie, Karl-Liebknecht-Strasse 24/25, D-14476 Potsdam-Golm, Germany; [e]Paul Scherrer Institut, Swiss Light Source, Photon Science Division, 5232 Villigen PSI, Switzerland; [f]Royal Institute of Technology, Theoretical chemistry and biology, Roslagstullsbacken 15, SE-10691 Stockholm, Sweden; [g]Institute of Nanotechnology, Spectroscopy and Quantum Chemistry, Siberian Federal University, 660041 Krasnoyarsk, Russia

This manuscript was compiled on September 6, 2018

**The phase diagram of water harbours controversial views on underlying structural properties of its constituting molecular moieties (1), its fluctuating hydrogen bonding network (2) as well as pair-correlation functions (3). In this work, long energy-range detection of the X-ray absorption allows us to unambiguously calibrate the spectra for water gas, liquid and ice by the experimental atomic ionization cross section. In liquid water we extract the mean value of 1.74 ± 2.1% donated and accepted hydrogen bonds per molecule pointing to a continuous distribution model. In addition, resonant inelastic X-ray scattering with unprecedented energy resolution also supports continuous distribution of molecular neighbourhoods within liquid water, as do X-ray emission spectra once the femtosecond scattering duration and proton dynamics in resonant X-ray–matter interaction are taken into account. Thus, X-ray spectra of liquid water in ambient conditions can be understood without a two-structure model, whereas the occurrence of nanoscale length correlations within the continuous distribution remains open.**

Water | X-ray | Spectroscopy |

Since the electronic structure of water molecules can support both 2- and 4-fold coordination in their molecular interaction, both a view of continuous distribution of molecular moities (homogeneous view) (4–10) and a view of oscillations between separate distinct phases (heterogeneous view) (11–15) of liquid water can be envisaged. The heterogeneous view foots strongly on the consideration that in the supercooled regime statistical response functions diverge at 228 K, introducing a liquid-liquid critical point, that would terminate the transition line between high-density and low-density liquid phases (16). In consequence, fluctuations between patches of different intermolecular organization could exist up to 320 K in the ambient regime (17), which is in striking contrast to the homogeneous view of liquid water at ambient conditions. This two-phase model of liquid water has been repeatedly promoted by the interpretation of X-ray spectroscopic findings (18) (and references therein), but the spectra have also been interpreted on the basis of homogeneous water models (19–21).

## X-ray absorption spectra

Soft X-ray Oxygen 1s X-ray absorption spectroscopy (XAS), electron energy loss spectroscopy (EELS), and equivalent information from hard X-ray Raman scattering (XRS) for the Oxygen 1s excitations has been utilized to characterize the various phases of water (14, 22–27). In these studies, integral or area-normalization within the measured spectral range between 530 eV and 550 eV has typically been employed, with the aim to fulfill the theoretical concept of the f-sum rule (28) present for an ideal – complete – spectral range with clearly discernible bound and continuum states. Combining simulations with area normalization, a significant signature of broken hydrogen bonds in liquid water has been postulated (14) based on the observation of increasing intensity in the $4a_1$ LUMO line (I in Fig. 1 (c)) along transitions from ice to liquid water and finally gas phase. However, in the f-sum rule normalization, the decrease of intensity in the pre-edge region is exactly counterbalanced by a intensity gain in other regions within the normalization range, because the spectrum integral is forced to a fixed value. Therefore, employing area-normalization within the range of 530 eV and 550 eV to fulfil the f-sum rule induces a trade-off in spectral intensity within the experimentally accessed energy range. Moreover, this trade-off is limited to the normalization range, which is unjustified as such spectra do not meet each other at the end of the integration interval (see

### Significance Statement

Water is the matrix of life and behaves anomalously in many of its properties. Since Wilhelm Conrad Röntgen, two distinct separate phases have been argued to exist in the liquid generally – or at least in the supercooled regime - competing with the other view of continuous distribution models. The interpretation and modeling of X-ray spectroscopic results has leant repeatedly towards two phase arguments for the liquid phases of water. We conducted a quantitative and high resolution X-ray spectroscopic multi-method investigation and analysis (X-ray absorption, X-ray emission, and resonant inelastic X-ray scattering). We find that all known X-ray spectroscopic observables can be fully and consistently described with continuous distribution models of near-tetrahedral liquid water at ambient conditions with 1.74 ± 2.1% H-bonds per molecule.

The RIXS experiment was done by JN, MF, SE, RMJ, AP, MD, XL, DMN, TS, and AF, and data handled by JN, SE, and AP. The XRS experiment was done by CJS and JN, and the data handled by CJS. The XES experiment was done by SE, RMF, JN, MF, AP and the data was handled by SE. The XES simulations were done by CJS~~, MO~~ and KG and analysed by JN. The manuscript was written by JN, AF~~, MO~~ , FG, AP, VVDC, and VK. The research was planned by AF, JN~~, MO~~ , AP, and FG and directed by AF. All authors have been given the option to comment the manuscript.

Authors declare no competing interest

[1]To whom correspondence should be addressed. E-mail: alexander.foehlisch@helmholtz-berlin.de

Fig. S1).

In Fig. 1(a),(b) and (c) we present the phase diagram of water in relation to Oxygen 1s XAS spectra obtained from saturation-free hard X-ray Raman spectroscopy for ice and liquid, and electron-energy-loss spectroscopy for gas from Ref. 22 (raw data after subtraction of constant background), where we follow the idea presented in Refs. 27, 29 and replace the f-sum rule normalization with f-density ($\mathrm{d}f(E)/\mathrm{d}E$) normalization at the high-energy end (see also Fig. S2). Panels (b) and (c) represent scans of gas, liquid and ice. The use of f-density normalization is based on the reasoning that at the sudden limit (a fast photoelectron) the photoionization cross section is an atomic property, independent of sample composition and varying bonding situations. Thus f-density links XAS state populations of different materials and molecules via fundamental core–continuum transition properties in the most reliable way when the spectra reach the asymptotic regime.

Most notably, the intensity variation of the LUMO $4a_1$ pre-edge feature in region I of Fig. 1(b) under f-density normalization yields a quantitative measure of donated hydrogen bonds per molecule for the liquid, ice and gas phase of water. With 0 donated bonds for gas and 2 donated bonds for ice and a linear dependence between the structural parameter average and line intensity, we derive from the f-density normalized pre-peak intensities (Table S1) of liquid water an average of 1.74 ± 2.1% donated hydrogen bonds per molecule (see SI for discussion about the error estimate). This value is significantly closer to the 2 donated bonds of ice than the previously derived 1.1 (see Ref. 14 and SI) bonds per molecule~~, that results from spectra normalized to the reduced photon energy range of 550 eV, or other values depending on the chosen short range integration interval.Therefore, breaking of H-bonds between ice and liquid water occurs to a lesser degree than previously assumed.~~ **. With the interpolation method used here, for the spectra normalized in area up to 550 eV the value 1.67 is obtained. We conclude that breaking of H-bonds between ice and liquid water occurs to a lesser degree than concluded in Ref. 14.**

Quantitative line-intensity–structural-parameter correlation based on a first principles liquid simulation (30) can now be considered (Fig. 1(d)). For the pre-edge LUMO $4a_1$ (region I), intensity is anticorrelated to donated (D) and accepted (A) hydrogen bonds, but correlated to the sum angular deviation from tetrahedrality ($\Delta_a$) as well as furthest-nearest difference ($\Delta_d$) of the closest four neighbouring O sites.

For the post edge region III, we observe in f-density normalization a strong rise of spectral intensity going from liquid water towards ice structures, and no contributions in gas (Fig. 1(c)). Since the post edge of condensed water resides in the continuum (O1s binding energy in liquid $\mathrm{BE}_{O1s}$=538.21 eV (31)), its interpetation must not foot on bound state arguments, but can only be attributed to continuum scattering resonances (shape resonances) reflecting structural order (26). For the shape resonance at $\mathrm{hv}_{in}$ ~542 eV the second and third nodes of the scattered electron wave function with $\mathrm{E}_{kin}$=$\mathrm{hv}_{in}$-$\mathrm{BE}_{O1s}$= 542 eV - 538.21 eV ~ 4 eV show characteristic lengthscales of 3.1 Å and 4.6 Å, respectively. This makes the shape resonance region sensitive to the first and the second solvation shell radii (32), and the corresponding potential barrier height, values of which (from digitization) are presented in Table S2. The interpretation of the post-edge (III) as a shape resonance has been proposed to originate from the nearest neighbours (33). We attribute the post-edge (III) intensity behaviour to be caused by a shape resonance that is due to both first and second solvation shells. This conclusion is supported by matching the solvation shells and their radial-distribution-function (RDF) peak heights as a measure of the mean barrier height. This continuum scattering resonance in liquid and ices is responsible for the artificial suppression of the pre-edge when area normalization from 530 eV to 550 eV is used.

The ~~notable~~ **complete** break-down of the hydrogen-bond network of water in the gas phase is reflected in raising pre-edge (I) (Fig.1 (b) and (c)), whereas the post-edge (III) disappears due to loss of solvation-shell order needed for the

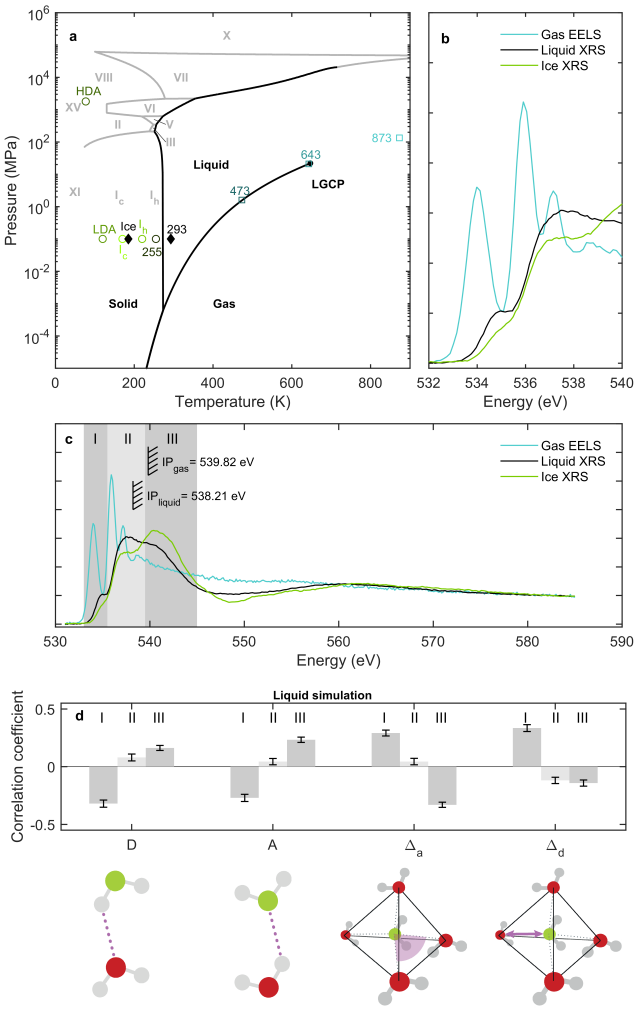


**Fig. 1.** (a) Schematic phase diagram of water in relation to Oxygen 1s X-ray absorption spectra obtained from saturation-free hard X-ray Raman spectroscopy. (b,c) We replace the f-sum rule normalization with f-density ($\mathrm{d}f(E)/\mathrm{d}E$) normalization at mean ionization cross section between 580 eV and 585 eV for gas, liquid and ice. Region I: LUMO $4a_1$ pre-edge feature. Region II: overlaping LUMO+1 $2b_2$ and continuum features. Region III: Continuum region, with shape resonance ($\mathrm{hv}_{in}$ ~542 eV) from second shell O–O continuum scattering resonance. (d) Line-intensity–structural-parameter correlation coefficients based on first principles liquid simulation (30) for regions I-III (lesser correlations Fig. S4): donated (D) and accepted (A) hydrogen bonds, sum angular deviation from tetrahedrality ($\Delta_a$) and furthest-nearest difference ($\Delta_d$) for the closest four neighboring O sites.

shape resonance. In the language of quantitative line-intensity–structural-parameter correlation coefficients based on first principles liquid simulation (30) in Fig. 1(d) this is expressed as dominant anti-correlation between the shape-resonance intensity in region (III) with the sum angular deviation from tetrahedrality ($\Delta_a$) and correlation with donated (D) and accepted (A) hydrogen bonds.

## Resonant inelastic X-ray scattering spectra

Next we turn to liquid water by studying O K-edge resonant inelastic X-ray scattering (RIXS) (Fig. 2). We focus on the bound excitations to $4a_1$ LUMO (region I), to states at the main edge, and core ionization continuum through the scattering resonance. In this work the spectra were recorded with unprecedented resolving power (>10000) by using the SAXES spectrometer (34) at the ADRESS beamline (35) on the Swiss Light Source at Paul Scherrer Institut. Finally we present XES spectra taken at numerous incident energies approaching the sudden core ionization, measured with instrument of more modest resolution (See Fig. S3 for complete XES spectra).

Comparing the RIXS spectra of electronic loss features (Fig. 2 panel b) taken at 545 eV to those excited to the shape resonance at ∼540 to 542 eV (region III) a noticeable shift of +0.20 eV is observed, due to different coupling and screening of a fast photoelectron, and a slow resonantly trapped photoelectron. Trivially, for both continuum excitations, photoionization leads to no vibrational excitations in the quasielastic region (Fig. 2 panel (c)), as the ionized system can not return to the neutral ground state. We note that XES spectra with differing energy calibrations have been reported (36, 37); we calibrated with respect to data from Ref. 36.

As seen in Fig. 2 panel (c), excitation into the electronic bound state $4a_1$ LUMO of liquid water yields strong vibrational excitations next to the elastic line. These excitations represent the projection of the core-hole-state-propagated wavepacket back onto the molecular ground state potential energy surface (38–40). For the main edge the experimental vibrational progression in liquid water shows significant shortening over the gas phase, a sign of suppression to exhibit the symmetric stretch mode in the liquid environment. **Note to A&A: we do not plot main edge comparison. I ignored your comment here, we show the 4a1 progression in Fig 3. We should cite a gas phase paper here.**

In Fig. 3 we thus show side by side the experimental vibrational losses via the electronic bound state $4a_1$ LUMO gas phase water (Fig. 3 (a)) and of liquid water (Fig. 3 (d)). The ground state potential energy surface as a function of O–H distance extracted from experimental RIXS for the gas phase, using a Morse-potential-cut approach as has been used in Ref. 40, are shown for gas (Fig. 3 (c)). The vibrational progressions for both gas and liquid water show only a single dominant O–H stretch mode. In the gas phase this mode persists as a distinct peak up to very high vibrational quantum numbers. In the liquid phase, however, broadening towards higher vibrational quantum numbers sets in, which is caused by a statistical distribution of the liquid local environments. No indication for two energetically shifted, distinct O–H stretch frequencies indicative of a two-phase model can be detected.

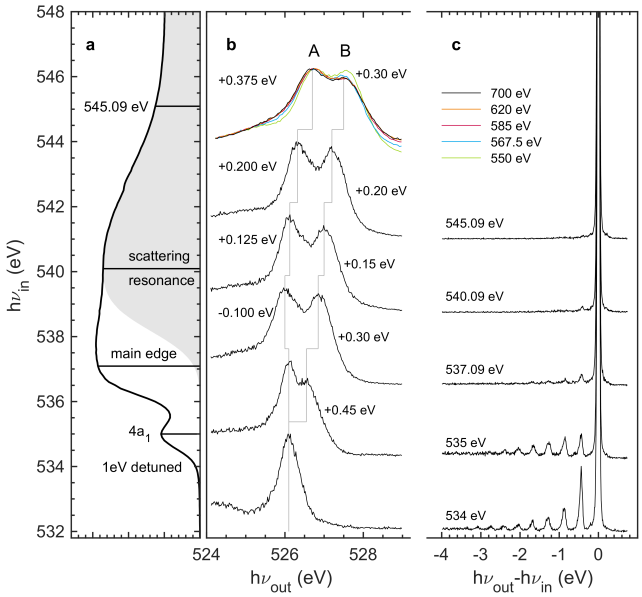


**Fig. 2.** Liquid water at ambient conditions: (a) Oxygen 1s X-ray absorption in direct relation to O1s resonant inelastic X-ray scattering with sub-natural-line-width spectral resolution of 50 meV. (b) $1b_1$ HOMO electronic losses at various incident-photon energies normalized to respective maximum value. (c) vibrational losses normalized to main elastic peak height mapping the ground state potential energy surface along selected coordinates. Shaded area is the contribution of photoionization continuum with an ionization threshold built up from step functions of each of the manifold of the molecular species in liquid water.

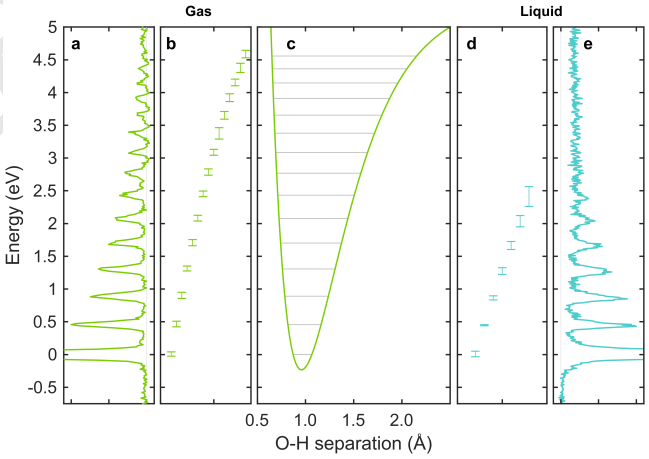


**Fig. 3.** Ground state vibrational levels along the O–H coordinate of molecular moities present in gas phase (a,b) and liquid water at ambient conditions (d,e) extracted from the vibrational progressions of O1s sub-natural linewidth RIXS excited at the $4a_1$ LUMO X-ray absorption resonances, respectively. Broadening of vibrational progression in the liquid phase from continuous distribution of molecular configurations (d). No broadening in the single $H_2O$ molecule configuration in the gas phase (b) and the single potential energy surface along the O-H coordinate extracted from the Morse potential (c).

## X-ray emission spectra

Finally let us turn to the RIXS electronic losses in Fig. 2 (b), where the $1b_1$ emission line in the water O K-edge X-ray emission spectrum (XES) appears as a double peak in condensed phases (18). This splitting (A,B in Figure 2 (b)) has been promoted as a fingerprint of two distinct structural motifs

within the liquid phase (41), which is opposed by arguments of nuclear dynamics causing this effect (20, 21, 42). In the latter view it is important to realize that the splitting at ionization may have different origin compared to those of different resonant states due to different core-hole-state potential energy landscapes, and therefore possibly different dynamics.

The XES spectrum taken at 550 eV and above in Fig. 2 (b) (see Fig. S3 for full spectra) manifests the photon energy dependence in the continuum, which indicates the ionized electron still to be coupled to the decay. Matching the behaviour of the XAS spectra in Fig. 1 (c), at 585 eV and above the convergence of the XES spectral shape is observed, with a result of significantly more "ice-like" spectrum recorded using an X-ray tube (43) (Figure 1 in the reference) than at lower energies. This finding alone questions the use of the split peak components as indicators of two liquid phases, as this would imply solid ice at liquid nitrogen temperature to have these phases.

Our Bethe-Salpeter equation XES simulations (average 1.88 accepted and donated hydrogen bonds per molecule) account for core-hole dynamics of different durations (Fig. 4(a)). They show that the formation of the lower-energy split component requires core-ionized-state dynamics in the long and the short O–H bonds to take place between ionization and X-ray emission. This dynamical interpretation also explains why slower-moving deuterated samples show a reduced peak A (21, 37, 44–47). For resonant excitations and ionization, the origin of the split peak may be different, as the potential energy surfaces governing the dynamics, in principle, may differ from each other. Still the dynamic view is consistent with spectra obtained at detuned $4a_1$ resonance, where the electronic loss feature appears as a single line that develops into a double peak when tuned to the $4a_1$ and above. This is understood as an indication of longer effective scattering duration.

The split-peak has a weak dependence to underlying structure seen in the branching ratio A/B, similarly to what we have established for the chain length dependence in liquid alcohols (48). We performed (Fig. 4) a full statistical analysis linking the the A'/B' branching ratio to the continuum RIXS simulation for liquid water. We reveal how A'/B' increases by increased hydrogen bonding (donated D, accepted A) and decreases by increased deviations from tetrahedrality ($\Delta_a$ angular, $\Delta_d$ distances) of the environment (Fig. 4 (b)). These findings are in full agreement to experiments presented here and earlier: the lower-energy component (A in Figure 2) of the split peak in water is reduced in higher temperatures of the liquid (21, 44) and increased upon freezing (21, 43). The occurance of the split-peak of water XES itself is a dynamical effect, equivalent to i.e. alcohols, where the branching ratio picks up some weak but notable statistical trend to structural parameters, as shown in our simulations.

## Conclusions

When putting the information from the three spectroscopies X-ray absorption, resonant inelastic X-ray scattering (RIXS) and non resonant X-ray emission together we can proceed to conclusions. Analysis of the X-ray absorption across the phase diagram of water using f-density normalization reveals for liquid water 1.74 donated hydrogen bonds per molecule, being closer to the 2 donated hydrogen bonds in 4-fold coordinated tetrahedral ice than previously derived from short range spectral normalization. In this quantitative normalization the occurance of a continuum scattering or shape resonance representing the structural order of the Oxygen-Oxygen next neighbour coordination shells in the liquid and ice is established. This shape resonance is absent in gas and supercritical phases, since the number of hydrogen bonds is reduced.

Consequence of this quantitative understanding is that resonant inelastic X-ray scattering via the $H_2O$ LUMO $4a_1$ state is sensitive to all bonding arrangements that might be present in liquid water. Potential-energy-surface mapping with sub-natural line width RIXS on gas phase and liquid water finds no indication of two distinct molecular potentials. ~~If two motifs of water existed, the two distinct potentials should give a split in RIXS vibrational progressions, which even high up in the vibrational progression is not observed at spectral bandwidth of 50 meV.~~ **A split peak in RIXS vibrational progression would be a potential (but not conclusive) indication of two structural motifs. This kind of behavior is not observed at spectral bandwidth of 50 meV.** Instead we observe gradual broadening in a continuous way, which strongly supports

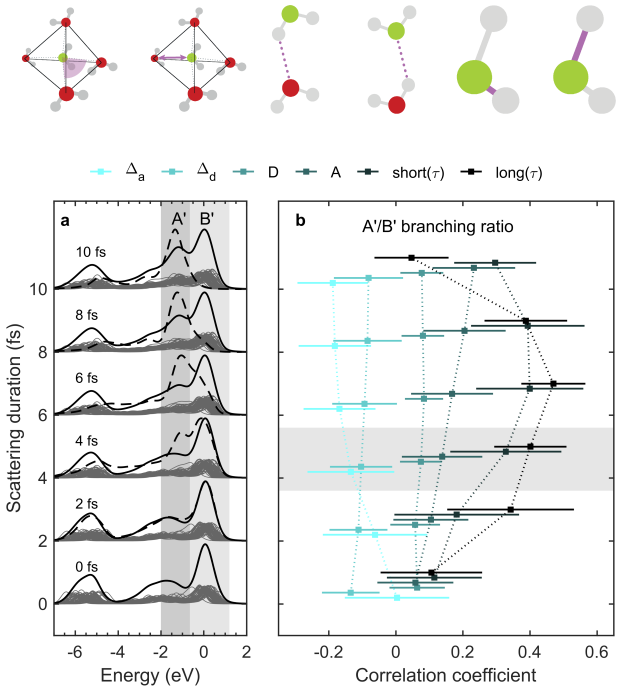


**Fig. 4.** Formation of a split-peak in the $1b_1$ HOMO electronic losses from ultrafast molecular relaxation during the femtosecond natural-lifetime of the O1s core ionized intermediate state of RIXS in the sudden limit (X-ray emission, XES). (a) MD simulation of O1s RIXS under sudden limit as a function of scattering duration $\tau = 0, 2, 4, 6, 8, 10$ fs (individual decay-time averaged spectra scaled x0.2). The instantaneous average is shown as dashed line. (b) Correlation coefficients between the split-peak branching ratio (A'/B') from core hole dynamics (time-averaged integrated XES spectra) and structural parameters at the site of ionization. The error bars represent 1000-fold bootstrap re-sampling. Weak correlation of split-peak intensity sum branching ratio (A'/B') to angular deviation from tetrahedrality ($\Delta_a$), to the furthest-nearest difference ($\Delta_d$) for the closest four neighboring O sites, and to donated (D) and accepted (A) hydrogen bonds (the parameters are calculated at the moment of ionization). Stronger correlation to the elongation of the short O-H bond during the scattering process (short($\tau$)). Strongest correlation to the elongation of the long O–H bond during the scattering process (long($\tau$)).

the continuum model description of liquid water.

In non-resonant X-ray emission spectroscopy the splitting of the HOMO $1b_1$ state into a split peak has been promoted as a signature of two structural motives in liquid water. The experimental finding, that in the sudden limit (at high incident energy) the photoelectron decouples from decay yielding an ice-like emission spectrum rules emission spectrum as an evidence for two structural motives in the liquid. This reasoning roots on similarity of the emission spectra and the fact that ice does not have two liquid phases. Additional support is given by a liquid 64-water simulation with periodic boundary conditions including both structural variation and core-hole-state dynamics on equal footing, being in line with numerous previous simulations. In particular, split peak branching ratio relationships show that dynamics plays a key role in the formation of the $1b_1$ double peak, with a very weak dependence on the starting structure.

Thus, the findings of X-ray spectroscopic tools are in full agreement with the continuous distribution model of liquid water structure equally reported in the vast number of non-X-ray based investigations of water.

**Supporting Information (SI).** Available as a separate file.

## Materials and Methods

**Experiments.** The hard X-ray Raman experiment for liquid water and ice was performed using the X-ray Raman scattering spectroscopy instrument (49) at the beamline ID20 of ESRF. The momentum transfer used for detection was $q = 2.6 \pm 0.6$ Å$^{-1}$. The scans for the ice sample were performed from below and from above to confirm that radiation damage does not introduce an error in the data (see Fig. S2). For the experiment, the liquid water sample was filled into a custom-made flow cell (50), and the ice sample was prepared *in situ* in a 2 mm quartz capillary continuously cooled by using a cryostream (Oxford cryosystems) at approximately at -88 °C. For both samples, milli-Q water was used. The raw data was handled as described in (51). The intensity integral values in the data are presented in Table S1. There are also problems in using f-sum rule due to varying completeness of the set of accessible final states (52), here seen as mismatch between gas phase and condensed phases. The XAS of Fig. 3 was recorded using the flat-jet transmission NEXAFS setup (53) at BESSY-II. The ionization step of Fig. 3 is taken from gaussian-shaped-assumed O1s photoline (31) with width from Ref. 54.

The RIXS experiment was performed with the SAXES spectrometer (34) at the ADRESS beamline (35) on the Swiss Light Source at Paul Scherrer Institut. We utilized a flow-cell separating the sample from the vacuum by a $Si_3N_4$ window of 150 nm thickness with a ∼10 nm Au coating. The energy calibration was based on $O_2$ spectrum (38). Due to breakdown of the windows in irradiation, the cell was moved between the spectra. To avoid errors from this procedure, these individual scans were shifted to the same energy by using a fit to the elastic line before joining them. The data in the electronic loss region is presented with larger energy binning for improved statistics.

Line positions and widths from the RIXS spectra were defined by a fit using Voigt profiles with a shared Lorentzian contribution, which was varied in the process. The Gaussian broadenings $\sigma$ of the lines were treated as independent parameters, and are reported as widths in Figure 3. The elastic line was included to the fit only up to the level of other lines, meaning that the top part of the true elastic line was ignored. This is motivated by the line shape not being a Voigt profile.

For the obtained line positions, we performed a fit using the effective mass of $\mu$=0.94 a.m.u. in a one-dimensional Morse potential

$$V(r) = D_e(1 - \mathrm{e}^{-a(r-r_0)})^2 \qquad [1]$$

with eigenvalues

$$E_i = h\nu(i+1/2) - \frac{(h\nu(i+1/2))^2}{(4D_e)}, \quad \nu = \frac{a\sqrt{2D_e/m}}{2\pi} \qquad [2]$$

to obtain parameters $D_e$ and $a$. The position of the minimum $r_0$ is not obtainable from the data and was given the value 0.95 Å, when drawing the potential energy curve for gas.

The XES experiment for photon energies 550 eV and above was performed at the beamline U49-2/PGM-1 in BESSY-II by using the setup described in Ref. (55). The XES data was calibrated by using the spectrum at 550.1 eV reported in Ref. (36).

**XES Simulations.** We performed a statistical simulation on liquid water using Car-Parrinello molecular dynamics (CPMD) for simulation cell of 64 molecules within the CPMD software (version 3.11) (56). Ground state AIMD of the pure liquid was equilibrated for at least 6 ps (starting from classical force field models) at ambient conditions at 300 K in the NVT ensamble using the Car-Parrinello algorithm (57) with a time-step of 0.1 fs and a fictition energy mass of 500 au. The model consists of 64 water molecules in a cubic simulation cell (a=12.4170 Å). All AIMD simulations employed the gradient-corrected density functional, BLYP (58, 59), and a 85 Ry kinetic energy cut-off for the plane wave expansion of the Kohn-Sham wave-functions in combination with a pseudopotential description. For hydrogen a local pseudo-potential parametrized with one Gaussian was used (60). For oxygen, the norm-conserving pseudo-potentials were of Troullier-Martins type (61), expressed in the Kleinman-Bylander form (62). As a basis for considering dynamical effects in the X-ray emission spectrum simulations, we performed Born-Oppenheimer AIMD simulations for the core-ionized states of each molecule in a single snapshot of both solvents. This resulted in 64 trajectories of core-hole dynamics for liquid water. The dynamical response to the core-ionization was simulated by continuing the ground state MD in the core-ionized state, but substituting one oxygen pseudopotential with a specially developed pseudopotential for oxygen with $1s^1$ occupation (63).

The XES spectra were evaluated using the Bethe-Salpeter equation (BSE) formalism as implemented in the OCEAN code (64, 65). For the XES calculations the electronic ground state calculations were performed using the Quantum ESPRESSO program package (66) and norm-conserving pseudopotentials obtained from the ABINIT distribution (67). For the calculation of the ground state electron density, we used Γ-point sampling and a $2 \times 2 \times 2$ K-point mesh for the evaluation of the used 1600 final states. Wave functions were truncated beyond a cutoff of 70 a.u. We evaluated the K$\alpha$ emission line separately for each of the 64 oxygen atoms in the simulation box of water separately along the respective excited state MD trajectory. The sampling along the core-hole induced dynamics trajectory was performed at 2 fs intervals up to 10 fs. We computed the XES $\sigma(T)$, accumulated up to time $T$, of ionized water as follows

$$\sigma(T) = \int_o^T \sigma_{\mathrm{ins}}(t) e^{-\frac{t}{\tau}} dt, \qquad [3]$$

$$\tau = \frac{1}{FWHM} = \frac{0.658}{0.16eV} = 4.11\mathrm{fs} \qquad [4]$$

The energy scale is relative to the ground state of the ion, and we averaged over all oxygen sites of the simulation box. The results with different upper limit $T$ for the integral are depicted in Figure 4, where the instantaneous averaged emission spectra are also shown.

In the analysis of XES, we refer to these parameters at the moment of ionization (before the core-ionized dynamics), except for bond lengths that are evaluated at the indicated time. The error limit is based on the standard deviation in 1000-fold bootstrap re-sampling technique.

**Standing-wave equation.** In atomic units, for a standing wave between $-R$ and $R$ the wave-vector of a free electron $k = \sqrt{2E}$ has to fulfill $k = n\pi/(2R)$, where $n = 1, 2, 3, ...$ For $E$ in eV and $R$ in Å, this yields

$$R = n\pi/(2 \times \sqrt{2E/27.211}) \times 0.529 \qquad [5]$$

for a standing electron wave to exist. The standing-wave condition mimics the condition for a scattering state to be trapped in the potential barrier by neighboring molecules.

**ACKNOWLEDGMENTS.** **We are grateful to prof. M. Odelius for providing us with an *ab initio* molecular dynamics simulation for core-hole dynamics.** We thank prof. J. Tse for providing us the XRS spectra of ice phases. S.E., R.M.J. and A.F. acknowledge funding from the ERC- ADG-2014 - Advanced Investigator Grant No. 669531 EDAX under the Horizon 2020 EU Framework Programme for Research and Innovation. Parts of this research were performed at the ADRESS beamline of the Swiss Light Source at the Paul Scherrer Institut with SAXES spectrometer in Villigen PSI, Switzerland. The work at PSI is supported by the Swiss National Science Foundation (SNSF) through the NCCR MARVEL, the Sinergia network Mott Physics Beyond the Heisenberg Model (MPBH) and a D-A-CH project (SNSF Research Grant No. 200021L 141325). X.L. acknowledges financial support from the European Community's Seventh Framework Programme (FP7/2007-2013) under Grant Agreement No. 290605 (PSIFELLOW/COFUND). AIMD simulations underlying the XES spectrum simulations were performed on resources provided by the Swedish National Infrastructure for Computing (SNIC). V.K. and F.G. acknowledge support within the State contract of the Ministry of Education and Science of the Russian Federation for Siberian Federal University for Scientific Research in 2017–2019 (Project No. 3.2662.2017), the Knut and Alice Wallenberg Foundation (Grant No. KAW-2013.0020), and Swedish Research Council (VR).

1. Ball P (2008) Water – an enduring mystery. *Nature* 452:291–292.
2. Stokely K, Mazza MG, Stanley HE, Giancarlo F (2010) Effect of hydrogen bond cooperativity on the behavior of water. *Proceedings of the National Academy of Sciences of the United States of America* 107:1301–1306.
3. Skinner LB, et al. (2013) Benchmark oxygen-oxygen pair-distribution function of ambient water from x-ray diffraction measurements with a wide q-range. *The Journal of Chemical Physics* 138(7):074506.
4. Sastry S, Debenedetti PG, Sciortino F, Stanley HE (1996) Singularity-free interpretation of the thermodynamics of supercooled water. *Physical Review E* 53:6144.
5. Smith JD, et al. (2004) Energetics of hydrogen bond network rearrangements in liquid water. *Science* 306:851–853.
6. Smith JD, et al. (2005) Unified description of temperature-dependent hydrogen-bond rearrangements in liquid water. *Proceedings of the National Academy of Sciences of the United States of America* 102:14171–14174.
7. Head-Gordon T, Johnson ME (2006) Tetrahedral structure or chains for liquid water. *Proceedings of the National Academy of Sciences of the United States of America* 103:7973–7977.
8. Clark GNI, Hura GL, Teixeira J, Soper AK, Head-Gordon T (2010) Small-angle scattering and the structure of ambient liquid water. *Proceedings of the National Academy of Sciences of the United States of America* 107:14003–14007.
9. Clark GN, Cappa CD, Smith JD, Saykally RJ, Head-Gordon T (2010) The structure of ambient water. *Molecular Physics* 108(11):1415–1433.
10. Kühne TD, Khaliullin RZ (2014) Nature of the asymmetry in the hydrogen-bond networks of hexagonal ice and liquid water. *Journal of the American Chemical Society* 136(9):3395–3399.
11. Palmer JC, et al. (2014) Metastable liquid-liquid transition in a molecular model of water. *Nature* 510(7505):385–388.
12. Sellberg JA, et al. (2014) Ultrafast x-ray probing of water structure below the homogeneous ice nucleation temperature. *Nature* 510:381–384.
13. Mishima O, Stanley HE (1998) The relationship between liquid, supercooled and glassy water. *Nature* 396:329–335.
14. Wernet P, et al. (2004) The structure of the first coordination shell in liquid water. *Science* 304(5673):995–999.
15. Huang C, et al. (2009) The inhomogeneous structure of water at ambient conditions. *Proceedings of the National Academy of Sciences of the United States of America* 106:15214–15218.
16. Poole PH, Sciortino F, Essmann U, Stanley HE (1992) Phase behaviour of metastable water. *Nature* 360:324.
17. Nilsson A, Pettersson LGM (2015) The structural origin of anomalous properties of liquid water. *Nature Communications* 6:8998.
18. Fransson T, et al. (2016) X-ray and electron spectroscopy of water. *Chemical Reviews* 116(13):7551–7569.
19. Prendergast D, Galli G (2006) X-ray absorption spectra of water from first principles calculations. *Phys. Rev. Lett.* 96(21):215502.
20. Odelius M (2009) Information content in o[1s] k-edge x-ray emission spectroscopy of liquid water. *The Journal of Physical Chemistry A* 113(29):8176–8181.
21. Fuchs O, et al. (2008) Isotope and temperature effects in liquid water probed by x-ray absorption and resonant x-ray emission spectroscopy. *Phys. Rev. Lett.* 100(2):027801.
22. Ishii I, McLaren R, Hitchcock AP, Robin MB (1987) Inner-shell excitations in weak-bond molecules. *The Journal of Chemical Physics* 87:4344.
23. Tse JS, et al. (2008) X-ray raman spectroscopic study of water in the condensed phases. *Phys. Rev. Lett.* 100(9):095502.
24. Sahle CJ, et al. (2013) Microscopic structure of water at elevated pressures and temperatures. *Proc. Nat. Acad. Sci.* 110:6301–6306.
25. Lehmkuhler F, et al. (2016) Intramolecular structure and energetics in supercooled water down to 255 k. *Phys. Chem. Chem. Phys.* 18(9):6925–6930.
26. Pylkkänen T, et al. (2010) Role of non-hydrogen-bonded molecules in the oxygen k-edge spectrum of ice. *The Journal of Physical Chemistry B* 114(11):3804–3808.
27. Pylkkänen T, et al. (2011) Temperature dependence of the near-edge spectrum of water. *The Journal of Physical Chemistry B* 115(49):14544–14550.
28. Johnson DL (1974) Local field effects and the dielectric response matrix of insulators: A model. *Phys. Rev. B* 9(10):4475–4484.
29. Krisch M, Sette F (2002) X-ray raman scattering from low z materials. *Surface Review and Letters* 9:969–976.
30. Niskanen J, et al. (2017) Disentangling structural information from core-level excitation spectra. *Physical Review E* 96:013319.
31. Olivieri G, Goel A, Kleibert A, Cvetko D, Brown MA (2016) Quantitative ionization energies and work functions of aqueous solutions. *Phys. Chem. Chem. Phys.* 18(42):29506–29515.
32. Finney JL, Hallbrucker A, Kohl I, Soper AK, Bowron DT (2002) Structures of high and low density amorphous ice by neutron diffraction. *Phys. Rev. Lett.* 88(22):225503.
33. Nilsson A, et al. (2010) X-ray absorption spectroscopy and x-ray raman scattering of water and ice; an experimental view. *Journal of Electron Spectroscopy and Related Phenomena* 177(2):99 – 129. Water and Hydrogen Bonds.
34. Ghiringhelli G, et al. (2006) Saxes, a high resolution spectrometer for resonant x-ray emission in the 400–1600 ev energy range. *Review of Scientific Instruments* 77:113108.
35. Strocov VN, et al. (2010) High-resolution soft X-ray beamline ADRESS at the Swiss Light Source for resonant inelastic X-ray scattering and angle-resolved photoelectron spectroscopies. *Journal of Synchrotron Radiation* 17(5):631–643.
36. Weinhardt L, et al. (2010) Resonant x-ray emission spectroscopy of liquid water: Novel instrumentation, high resolution, and the "map" approach. *Journal of Electron Spectroscopy and Related Phenomena* 177(2):206 – 211. Water and Hydrogen Bonds.
37. Lange KM, et al. (2012) X-ray emission from pure and dilute $h_2o$ and $d_2o$ in a liquid microjet: Hydrogen bonds and nuclear dynamics. *Phys. Rev. B* 85(15):155104.
38. Hennies F, et al. (2010) Resonant inelastic scattering spectra of free molecules with vibrational resolution. *Phys. Rev. Lett.* 104(19):193002.
39. Vaz da Cruz V, et al. (2017) A study of the water molecule using frequency control over nuclear dynamics in resonant x-ray scattering. *Phys. Chem. Chem. Phys.* 19(30):19573–19589.
40. Eckert S, et al. (2018) One-dimensional cuts through multidimensional potential-energy surfaces by tunable x rays. *Physical Review A* 97:053410.
41. Gallo P, et al. (2016) Water: A tale of two liquids. *Chemical Reviews* 116(13):7463–7500.
42. Odelius M (2009) Molecular dynamics simulations of fine structure in oxygen $k$-edge x-ray emission spectra of liquid water and ice. *Phys. Rev. B* 79(14):144204.
43. Gilberg E, Hanus MJ, Foltz B (1982) Investigation of the electronic structure of ice by high resolution x-ray spectroscopy. *The Journal of Chemical Physics* 76(10):5093–5097.
44. Tokushima T, et al. (2008) High resolution x-ray emission spectroscopy of liquid water: The observation of two structural motifs. *Chemical Physics Letters* 460(4–6):387 – 400.
45. Odelius M, et al. (2005) Ultrafast core-hole-induced dynamics in water probed by x-ray emission spectroscopy. *Phys. Rev. Lett.* 94(22):227401.
46. Weinhardt L, et al. (2010) Resonant x-ray emission spectroscopy of liquid water: Novel instrumentation, high resolution, and the "map" approach. *Journal of Electron Spectroscopy and Related Phenomena* 177(2–3):206 – 211.
47. Harada Y, et al. (2013) Selective probing of the oh or od stretch vibration in liquid water using resonant inelastic soft-x-ray scattering. *Phys. Rev. Lett.* 111(19):193001.
48. Schreck S, et al. (2014) Dynamics of the oh group and the electronic structure of liquid alcohols. *Structural Dynamics* 1(5):054901.
49. Huotari S, et al. (2017) A large-solid-angle X-ray Raman scattering spectrometer at ID20 of the European Synchrotron Radiation Facility. *Journal of Synchrotron Radiation* 24(2):521–530.
50. Sahle CJ, et al. (2015) A miniature closed-circle flow cell for high photon flux x-ray scattering experiments. *Journal of Synchrotron Radiation* 22(6):1555–1558.
51. Sahle CJ, et al. (2015) Planning, performing and analyzing X-ray Raman scattering experiments. *Journal of Synchrotron Radiation* 22(2):400–409.
52. Wheeler JA, Bearden JA (1934) The variation of the k resonating strength with atomic number. *Physical Review* 46:755 – 758.
53. Fondell M, et al. (2017) Time-resolved soft x-ray absorption spectroscopy in transmission mode on liquids at mhz repetition rates. *Structural Dynamics* 4:054902.
54. Winter B, Aziz EF, Hergenhahn U, Faubel M, Hertel IV (2007) Hydrogen bonds in liquid water studied by photoelectron spectroscopy. *The Journal of Chemical Physics* 126(12):124504.
55. Kunnus K, et al. (2012) A setup for resonant inelastic soft x-ray scattering on liquids at free electron laser light sources. *Review of Scientific Instruments* 83(12):123109.
56. (year?). CPMD, http://www.cpmd.org/, Copyright IBM Corp 1990-2008, Copyright MPI für Festkörperforschung Stuttgart 1997-2001.
57. Car R, Parrinello M (1985) Unified approach for molecular dynamics and density-functional theory. *Physical Review Letters* 55:2471–2474.
58. Becke AD (1988) Density-functional exchange-energy approxiation with correct asymptotic behavior. *Physical Review A* 38:3098–3100.
59. Lee C, Yang W, Parr RG (1988) Development of the colle-salvetti correlation-energy formula into a functional of the electron density. *Physical Review B* 37:785–789.
60. Giannozzi P (1993) Unpublished.
61. Troullier N, Martins JL (1991) Efficient pseudopotentials for plane-wave calculations. *Physical Review B* 43:1993–2006.
62. Kleinman L, Bylander DM (1982) Efficacious form for model pseudopotentials. *Physical Reviev Letters* 48:1425–1428.
63. Cavalleri M, Odelius M, Nordlund D, Nilsson A, Pettersson LGM (2005) Half or full core hole in density functional theory x-ray absorption spectrum calculations of water? *Phys. Chem. Chem. Phys.* 7:2854–2858.
64. Vinson J, Rehr JJ, Kas JJ, Shirley EL (2011) Bethe-salpeter equation calculations of core

excitation spectra. *Phys. Rev. B* 83(11):115106.
65. Gilmore K, et al. (2015) Efficient implementation of core-excitation bethe–salpeter equation calculations. *Computer Physics Communications* 197:109 – 117.
66. Giannozzi P, et al. (2009) Quantum espresso: a modular and open-source software project for quantum simulations of materials. *Journal of physics: Condensed matter* 21(39):395502.
67. Gonze X, et al. (2009) Abinit: First-principles approach to material and nanosystem properties. *Computer Physics Communications* 180(12):2582–2615.